Solution structure of NEMO zinc finger and impact of an anhidrotic ectodermal dysplasia with immunodeficiency-related point mutation.

Florence Cordier, Emilie Vinolo, Michel Véron, Muriel Delepierre, Fabrice Agou

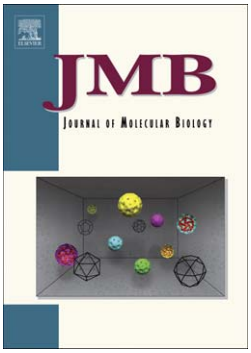

Solution structure of NEMO zinc finger and impact of an anhidrotic ectodermal dysplasia with immunodeficiency-related point mutation

Florence Cordier, Emilie Vinolo, Michel Véron, Muriel Delepierre, Fabrice Agou

PII: S0022-2836(08)00095-8
DOI: doi: 10.1016/j.jmb.2008.01.048
Reference: YJMBI 60155

To appear in: *Journal of Molecular Biology*

Received date: 27 September 2007
Revised date: 14 January 2008
Accepted date: 18 January 2008

Please cite this article as: Cordier, F., Vinolo, E., Véron, M., Delepierre, M. & Agou, F., Solution structure of NEMO zinc finger and impact of an anhidrotic ectodermal dysplasia with immunodeficiency-related point mutation, *Journal of Molecular Biology* (2008), doi: 10.1016/j.jmb.2008.01.048

Solution structure of NEMO zinc finger and impact of an anhidrotic ectodermal dysplasia with immunodeficiency-related point mutation

Florence Cordier[1*], Emilie Vinolo[2], Michel Véron[2], Muriel Delepierre[1] & Fabrice Agou[2*]

[1]Unité de RMN des Biomolécules and [2]Unité de Régulation Enzymatique des Activités Cellulaires, CNRS URA 2185, Département de Biologie Structurale et Chimie, Institut Pasteur, 25/28 rue du Dr. Roux, 75724 Paris Cedex 15, France

[*]To whom correspondence should be addressed: fcordier@pasteur.fr or fagou@pasteur.fr

Running title: EDA-ID-related mutation in NEMO zinc finger

Word count:	11512
Total character count:	60994
Page count:	2
File:	nemoZF_cordier_revised.doc
Last changed:	28.01.08 18:01

Abstract

The regulatory NEMO (NF-κB essential modulator) protein plays a crucial role in the canonical NF-κB signaling pathway notably involved in immune and inflammatory responses, apoptosis and oncogenesis. The regulatory domain is located in the C-terminal half of NEMO and contains a classical CCHC-type zinc finger (ZF). We have investigated the structural and functional effects of a cysteine to phenylalanine point mutation (C417F) in the ZF motif, identified in patients with anhidrotic ectodermal dysplasia with immunodeficiency. The solution structures of the wild type and mutant ZF were determined by NMR. Remarkably, the mutant adopts a global ββα fold similar to that of the wild type and retains thermodynamic stability, i.e. the ability to bind zinc with a native-like affinity, although the last zinc-chelating residue is missing. However, the mutation induces enhanced dynamics in the motif and leads to an important loss in stability. A detailed analysis of the wild type solution structure and experimental evidences lead to the identification of two possible protein-binding surfaces that are largely destabilized in the mutant. This is sufficient to alter NEMO function since functional complementation assays using NEMO-deficient pre-B and T lymphocytes show that full-length C417F pathogenic NEMO leads to a partial to strong defect in LPS, IL-1β and TNF-α-induced NF-κB activation, respectively, as compared to wild type NEMO. Altogether, these results shed light onto the role of NEMO ZF as a protein-binding motif and show that a precise structural integrity of the ZF should be preserved to lead to a functional protein-recognition motif triggering full NF-κB activation.

Keywords

NF-κB / NEMO / zinc finger / EDA-ID / NMR

Introduction

NF-κB transcription factors play a central role in many physiological processes including immune and inflammatory responses, cell adhesion, apoptosis and oncogenesis [1]. In unstimulated cells, they are sequestered in the cytoplasm by inhibitory molecules of the IκB family. Upon activation by a wide range of stimuli such as the proinflammatory cytokines TNF (tumor necrosis factor)-α and IL (interleukin)-1β or the endotoxin LPS (lipopolysaccharide), the IKK (IκB kinase) complex is activated. Although the latter was previously thought to be always present as a tripartite complex, it is now appreciated that it is heterogeneous and consists of several homo- and hetereodimeric complexes between the serine/threonine kinases IKKα and IKKβ and the critical regulatory subunit called NEMO (NF-κB essential modulator) or IKKγ [2]. When activated, the kinases phosphorylate the inhibitory IκB proteins, which are rapidly modified by K48 polyubiquitin chains and degraded by the 26S proteasome. This subsequently enables the NF-κB transcription factors to translocate into the nucleus and regulate target gene transcription.

Although lacking any catalytic activity, NEMO is essential to the canonical NF-κB pathway, as cells that do not express the protein are unable to activate the pathway in response to most stimuli [3, 4]. Recently, NEMO was also shown to be required for the interferon regulatory factor (IRF) signaling pathways through activation of the IRF7 and IRF3 transcription factors [5]. Moreover, a few years after its discovery, several rare human diseases have been linked to mutations in the *NEMO* gene located on the X chromosome (See [6] for a review). Amorphic mutations in NEMO are associated with incontinentia pigmenti (IP), a dominant disorder that is lethal *in utero* in males whereas heterozygous females present soon after birth variable abnormalities principally of the skin, but also of the eyes, teeth, hair and central nervous system [7]. Most IP patients carry a common rearrangement of

the *NEMO* locus leading to a large truncation of the protein and a complete absence of NF-κB activation [8]. Hypomorphic mutations in NEMO, that do not totally suppress the activation of the pathway, generally cause anhidrotic ectodermal dysplasia with immunodeficiency (EDA-ID) [9, 10, 11]. This recessive pathology only affects males. Beside the EDA developmental phenotype (namely rare conical teeth and absence or rarity of hair and sweat glands), EDA-ID patients present a severe immunodeficiency, which causes a high mortality in the first years of life due to recurrent opportunistic bacterial infections. A mutation in the *NEMO* stop codon has also been linked to a more severe form of EDA-ID associated with osteopetrosis and/or lymphoedema [9]. EDA and ID are not phenotypically linked since NEMO mutations were also found in patients only presenting an immunodeficiency, with in some cases conical teeth as the sole sign of EDA [12, 13, 14]. The spectrum of infections observed can be remarkably narrow, as two mutations have been recently identified in patients with the syndrome of susceptibility to mycobacterial diseases [15].

Based on its primary sequence, four structural motifs have been identified in NEMO (Figure 1(a)). The N-terminal half of the protein containing a long coiled-coil domain (CC1) is responsible for the interaction of NEMO with the IKK kinases. The C-terminal half is composed of another coiled-coil (CC2), a leucine zipper (LZ) and a zinc finger motif (ZF). This C-terminal domain constitutes the regulatory domain of NEMO, as it receives the activation signal from upstream molecules [16, 17], and subsequently transmits this activation to the kinases bound to the N-terminal domain. The latter mechanism remains unclear, even though several regulatory events have been implicated, including the oligomerization of NEMO via the CC2-LZ domain [18, 19], its posttranslational modification by phosphorylation [20, 21], K63 polyubiquitination [22, 23] and, more recently, the interaction with polyubiquitin chains linked through ubiquitin K63 via the CC2-LZ domain [24, 25].

Interestingly, several pathogenic NEMO mutations identified to date are located in the C-terminal regulatory domain, and in particular in the ZF motif [6]. Mutations found in the CC2-LZ domain are susceptible to alter the oligomerization of the protein, as we recently showed for an alanine to glycine substitution located in the CC2 motif and identified in an EDA-ID patient [26]. However, the exact role of the ZF motif has not yet been established. Although it is dispensable for NEMO self-association and for assembly of the IKK complex, NEMO ZF was shown to be required for full IKK activation in response to TNF-α and IL-1β [27], but also in response to UV radiations and genotoxic agents such as camptothecin and etoposide [28]. In addition, the ZF domain may be important for the ubiquitination of NEMO in response to TNF-α [22] or to a T cell receptor activation, for which K399 located in the domain was shown to be modified [23, 29]. NEMO ZF is of the CCHC type ($C\text{-}X_2\text{-}C\text{-}X_{12}\text{-}H\text{-}X_{1\text{-}5}\text{-}C$, where X indicates any amino acid), also found in proteins of the FOG (Friend of GATA) family, and may mediate protein/protein [30] rather than protein/DNA interactions. We have recently performed a modeling of the domain, which is predicted to form a ββα fold similar to classical zinc fingers [26].

Pathogenic mutations affecting the ZF motif include partial or complete deletion of this domain, or single point mutations (e.g. EDA-ID-D406V, IP-M407V). Interestingly, several EDA-ID patients were identified with a substitution of the highly conserved last zinc-chelating residue (C417R/F/Y, CCH<u>C</u>). The C417R mutation was shown to impair NF-κB activation in response to CD40 ligand [31], TNF-α or LPS [32]. However, a classical ZF lacking the last chelating residue (CCH<u>X</u>) retained the ability to bind Zn^{2+} and showed only a modest decrease in its DNA-binding affinity [33]. The question then arises whether the impairment of NEMO function was due to an improper folding of its ZF motif.

In this paper, we describe the structural and functional effects of the C417F mutation within the ZF motif of NEMO, which was identified in two unrelated patients with EDA-ID [9,

[11]. We determined the solution structure of the wild type ZF peptide (ZF-WT) by NMR and compared it to that of the pathogenic mutant (ZF-C417F) (Figure 1(b)), which remarkably retains a global structure very similar to that of the wild type. However, we observe a change in stability and dynamical behavior induced by the pathogenic C417F mutation that correlates with a partial to strong inhibition of the NF-κB pathway in response to LPS, IL-1β and TNF-α, respectively. Finally, our detailed analysis of NEMO ZF structure leads to the identification of two possible interfaces for protein-protein interactions, which are both altered in the mutant. Altogether, our results strongly suggest that integrity of NEMO ZF in term of structure, dynamics and stability need to be preserved to lead to a specific protein-recognition motif and to allow full NF-κB activation.

Results and Discussion

The wild type and mutant ZF peptides display zinc-induced folding with similar Zn^{2+} affinities

We first monitored the folding of the two ZF-WT and ZF-C417F peptides by NMR. In the absence of zinc, the amide/aliphatic region of the 2D-TOCSY spectrum of ZF-WT reveals very limited dispersion, with chemical shifts close to random coil values (Figure 2(a), red resonances), indicating that apo-ZF-WT is not folded. Addition of an equimolar amount (or slight excess) of $ZnSO_4$ induces a drastic change in the TOCSY spectrum. The resonances shift strongly to widely dispersed spectral positions, indicative of a well-folded Zn^{2+}-bound structure (Figure 2(a), black resonances). A few small peaks from the unfolded apo-state (unfolded residues A13-V23, Figure 2(a) red labels) can still be detected in the spectrum. The remaining unfolded peaks are invisible because of the fast amide proton exchange with water in the unfolded state at pH 7.3. Based on the ratio of peak intensities of isolated non-

exchangeable aromatic protons (H^{δ}(Y11) or H^{ε}(Y11)) in a 1D spectrum, 30 % of the WT peptide seems unfolded at most. In a NOESY experiment (220 ms, mixing time), the absence of cross-peaks between the folded and unfolded forms indicates either that they are not in exchange or that the exchange process is very slow (> 220 ms). Surprisingly, this apparent folded-unfolded equilibrium could not be shifted towards more folded state neither by addition of up to a 10-fold excess of $ZnSO_4$, nor by a variation of sample preparations and/or solvent conditions, i.e. pH 3.5-7.5, ionic strength (0-200 mM NaCl), buffer (Tris-HCl, phosphate), temperature (5 - 45°C), peptide concentration (0.1 – 1 mM), or even after a refolding procedure from strongly acidic (or basic) conditions at pH 2 (pH 10). The same behavior was observed with a longer construct of NEMO ZF (PPP-ZF-WT) including the proline-rich region (9 residues) preceding the ZF motif (not shown). The ZF-C417F mutant peptide is also unfolded in the absence of zinc, as judged from the weak spectral dispersion in the TOCSY spectrum (Figure 2(b), red resonances). Interestingly, equimolar addition of $ZnSO_4$ (or slight excess) induces some spectral changes to more dispersed positions, which denote folding of the peptide in spite of a missing zinc-chelating residue (Figure 2(b), black resonances). Numerous intense peaks from the unfolded apo-peptide (unfolded residues A13-I27, Figure 2(b) red labels) are still observed, corresponding to a population of 50 % at most. Moreover, the chemical shift differences between the folded and unfolded states (~ 0.5 – 1 ppm) and the presence of cross-peaks between the two forms in a NOESY experiment (220 ms, mixing time, Supplementary Data Figure S1) reflect a slow exchange process in the range of 2 – 220 ms. Again, no further folding could be obtained by up to a 20-fold excess of $ZnSO_4$, or by variations in sample preparations as described above for ZF-WT. At a first glance, most H^{N} and H^{α} proton chemical shifts of the zinc-bound form are somehow comparable to those of the wild type, indicating that the global fold of ZF-WT and ZF-C417F must be fairly similar. However, the narrower dispersion observed for the mutant ZF gives

evidence of a lower degree of secondary structure formation and thus of a less stable structure (see below).

To assess the quality of the two synthetic peptides, electrospray mass spectrometry and amino acid analysis were performed and showed correct mass, purity and amino acid composition (data not shown). The metal-binding stoichiometries were evaluated by flame atomic absorption spectroscopy. At a concentration of 5 μM, we found that both ZF-WT and ZF-C417F peptides bind a single zinc ion, with a ZF : Zn^{2+} stoichiometry of 1.0 ± 0.1 and 1.0 ± 0.2, respectively. Note that we could detect the presence of peptide aggregates invisible to the human eye for both synthetic peptides by dynamic light scattering, which is a very sensitive method to detect large species. These irreversible species detected in the absence and presence of Zn^{2+} were preferentially observed at a high concentration of peptide (1 mM). Thus, these species may be present under NMR conditions where a high concentration of peptide is required (0.1-1 mM).

Metal binding by ZF peptides commonly involves a single transition from an unfolded apo-protein to a well-folded metallo-protein [34]. The observation that folding is coupled to metal binding in ZF domains led to the development of folding-based probes for Zn^{2+} by fluorescence spectroscopy [35]. In a similar way, we estimated the affinity for zinc of the wild type and mutant ZF peptides by using the intrinsic fluorescence of Y11 as a folding probe. Excitation of apo-peptides at 285 nm yields a fluorescence emission maximum at 307 nm, characteristic of a tyrosine. Addition of an excess of zinc induces a significant increase of the emission intensity for ZF-WT (17%) and ZF-C417F (14%) with no change in the spectral shapes and wavelength maxima (Figure 3, *Inset*), indicating a change in the protein conformation that alters the local environment of Y11 in both peptides. The increase in fluorescence signal upon folding was therefore monitored during the $ZnSO_4$ titration, and the dissociation constant (K_D) and ZF : Zn^{2+} stoichiometry (n) were extracted from non-linear

least square fitting of the subsequent hyperbolic curve (Figure 3). A K_D of 0.3 ± 0.1 μM with a stoichiometry of 1.0 ± 0.2 is obtained for ZF-WT at pH 7.3 and 25°C, which is similar to the values observed for ZF-C417F at the same pH and temperature (K_D = 0.7 ± 0.2 μM, n = 1.0 ± 0.2). Thus, the replacement of a zinc-chelating cysteine by a phenylalanine does not markedly affect the thermodynamic stability of the ZF, i.e. its ability to bind a zinc ion. To dissect the Gibbs free energy (ΔG) of the coupled zinc-binding/peptide-folding process into enthalpic (ΔH) and entropic (TΔS) contributions, we performed isothermal titration calorimetry on both peptides (data not shown). Only small differences between the WT and mutant peptides ΔΔH (1.1 ± 0.2 kcal.mol^{-1}) and TΔΔS (1.3 ± 0.3 kcal.mol^{-1}) were obtained at pH 7.4, ruling out the possibility of an entropy-enthalpy compensation phenomenon (e.g. solvent reorganization) to justify the similar affinity for zinc.

Solution structure of the wild type zinc finger of NEMO and comparison to classical fingers

The structure calculation was performed as described in Materials and Methods, from NMR data obtained at 25°C, and structural statistics are given in Supplementary Data Table S1. The structure of the wild type ZF is well defined, with a root mean square deviation (RMSD) of 0.26 and 0.82 Å on the backbone and heavy atoms, respectively, for the non-flexible residues F4-C26 (Figures 4(a,b)). It consists of a short antiparallel β-sheet, where β1 (F4-C5) and β2 (Q12-A13) strands are connected by a type IV β-turn (C_6PKC_9), and an α-helix (M16-E25), as identified by the PROMOTIF program [36]. This ββα fold is stabilized by tetrahedral coordination to a zinc ion involving the thiol groups of C6, C9 and C26 and the $N^{\varepsilon 2}$ atom of H22. The side chains of residues F4, C6, C9, Y11, A13, L19, H22 and C26 are particularly well defined in the NMR ensemble and form the hydrophobic core of the finger. The core is further stabilized by a strong horizontal stacking interaction between the aromatic

side chain of Y11 and the zinc ligand H22, as revealed by upfield shifts of the Y11 H^{δ} and H^{ε} proton resonances and by strong NOE connectivities between Y11 and H22 side chain protons.

The ββα scaffold of NEMO ZF is mainly dictated by the arrangement of the tetrahedral zinc coordination site and is therefore considerably similar to that of classical CCHH and CCHC fingers. Indeed, an RMSD in the range 0.7 – 1.5 Å on the backbone (residues 4-26) is generally found between NEMO and other ZF (e.g. see Figure 4(c)), in spite of a rather low sequence identity. The stabilization of the core via the highly conserved F4, L19 and H22 residues and an aromatic anchor (or more rarely a large hydrophobic residue) is a general feature of classical zinc fingers. However, the aromatic residue is commonly found at position 13 (NEMO numbering) where it is rather involved in edge-to-face packing to the zinc-chelating histidine H22 (e.g. USH-F9 (U-shaped finger 9, [30]), see Figure 4(c)). In more unusual cases (~ 10 %), like in NEMO ZF, this aromatic is found at position 11 where it can stack onto H22. This situation was originally reported in the CCHH-type even fingers of the human Y-encoded ZFY protein (e.g. ZFY-6 [37], Figure 4(c)). Such an arrangement (further referred as "aromatic swap") was shown to provide equivalent contributions to the hydrophobic core as the consensus aromatic at position 13, though with slight changes in the surface implicated in DNA recognition [38]. The importance of this aromatic anchor has already been documented [39]. Finally, the variability among classical fingers in the position of the last chelating residue (commonly 26 or 27) and its nature (His or Cys) leads to slight differences at the C-terminal end of the α-helix. In CCH$\underline{H}_{26/27}$ or CCH$\underline{C}_{26}$ type fingers, the α-helix extends up to or beyond the final chelating residue, whereas in CCH$\underline{C}_{27}$ fingers the helix ends shortly after position 24 and is pushed away from the turn connecting β1 and β2 in order to maintain correct tetrahedral Zn^{2+} coordination (Figure 4(c)). The conformation of this region was shown to be important for binding of FOG and USH

fingers to the transcription factor GATA [30, 40] (see below). Therefore, as shown in Figure 4(c), the structure of NEMO CCH$\underline{C}_{26}$ ZF is more similar to those of CCH$\underline{H}_{27}$ ZFY-6 and CCH$\underline{H}_{26}$ FOG-F3 than that of CCH$\underline{C}_{27}$ USH-F9.

Identification of two potential protein-binding surfaces in NEMO zinc finger

Classical zinc fingers are commonly found as tandem arrays in transcription factors where they act as sequence-specific DNA-binding modules [41], but some of them (often more widely dispersed in proteins and of the CCHC type) have been shown more recently to function as protein recognition motifs [42]. The isolated NEMO zinc finger is thought to be involved in protein-protein rather than protein-DNA interaction. Interestingly, the structure of NEMO ZF exhibits a large hydrophobic face, mostly defined by one side of the α-helix and the β1 strand (Supplementary Data Figure S2(b)), whereas the opposite face is essentially polar and consists of the very acidic side of the helix and the β2 strand (Supplementary Data Figure S2(a)). This observation, together with several experimental evidences detailed below, lead to the identification of two possible protein-binding surfaces.

The polar region around tyrosine Y11 and the acidic side of the α-helix. We recently had evidence of a close intercommunication between the ZF and the minimal oligomerization domain CC2-LZ in NEMO (Figure 1(a)). Indeed, a strong tyrosinate emission signal, which was attributed to Y11, was observed by fluorescence spectroscopy in a construct constituted of the CC2-LZ-ZF domain named "C-ter" [26], whereas this tyrosinate signal is absent in the isolated ZF (Figure 3, *Inset*). This suggests that the acidic face of the ZF encompassing Y11 (white contour in Supplementary Data Figure S2(a)) likely interacts with the numerous basic residues of the CC2-LZ. Moreover, the pathogenic D15V point mutation (D406V in hNEMO), identified in a patient with EDA-ID [10], further illustrates the functional importance

of this acidic surface in NEMO ZF, since it corresponds to the loss of a negatively charged residue as well as a helix N-capping hydrogen bond (NH(D17)···O^{δ}(D15)).

Classical zinc fingers typically recognize the DNA major groove bases via the N-terminal half of the α-helix [41]. However, even if only a few examples have been related so far [30, 40, 43], the interface involved in protein recognition and the binding mode seem to differ to a larger extent. Thus the acidic nature of NEMO ZF surface should lead to a specific binding mode. Additional experiments are currently in progress to validate and precise the interaction between the ZF and the CC2-LZ domains.

The hydrophobic face. A large hydrophobic cluster is found on the opposite side of the polar face (white contour in Supplementary Data Figure S2(b)). As it would be very unlikely that such a large hydrophobic patch remains exposed to the solvent in physiological conditions, this surface or part of it may constitute a second protein-binding site with a yet unknown upstream molecule. Lysine K8 (K399 in hNEMO numbering), which is modified by K63 polyubiquitin chains in response to a T cell receptor activation [23], is located on the edge of the hydrophobic surface and remains accessible to be ubiquitinated (Figures 4(a,b)). The functional importance of this surface is also exemplified by the M16V point mutation (M407V in hNEMO) identified in several patients with the severe IP disease [8].

The mutant ZF adopts a native-like bba fold

For the CCHF mutant ZF, initial structure calculations performed without zinc ion revealed that metal coordination could only arise from the thiol groups of C6 and C9 and the $N^{\varepsilon 2}$ atom of H22. As a single Zn^{2+} site was identified in this finger by flame atomic absorption spectroscopy, the metal ion was then included in the subsequent calculations, assuming a tetrahedral coordination but involving only these three chelating residues. No NOE violations greater than 0.25 Å was obtained and the structures were of higher quality

than when calculated without zinc. Considering that aspartate [44], glutamate, asparagine and glutamine can also conceivably act as zinc ligands, we tested the possibility of such a residue being the fourth ligand in the ZF-C417F peptide. From our structures and NOE data, it was evident that D15, D17, Q20 and E28 could not be involved in zinc coordination, as it would require an important structural rearrangement. E25 could not be involved either, as no α-helical or long-range NOE connectivities corresponding to such an arrangement could be detected beyond M24, indicating that the C-terminus E25-E28 is clearly disordered. More details on the final structure calculation are given in Materials and Methods and structural statistics in Supplementary Data Table S1.

The structure of the mutant ZF is rather well defined, with an RMSD of 0.31 and 0.78 Å on the backbone and heavy atoms, respectively, for the non-flexible residues F4-V23 (Figures 5(a,b)). It has the same ββα fold as the wild type, i.e. a small β-sheet (F4-C5, Q12-A13) and an α-helix (M16-V23), although it is maintained by a zinc coordination involving only three residues. Like in the WT peptide, numerous long-range NOE connectivities are observed between the side chains of F4, C6, C9, Y11, A13, L19 and H22, as well as a strong Y11/H22 horizontal stacking interaction, indicating that the packing of the hydrophobic core is largely preserved. However, the structure of ZF-C417F is highly disordered from residue V23 to the C-terminal E28. Due to this local disorder, which is not an artifact produced by a low density of constraints (see below for more details), the zinc-binding site is more accessible to the solvent than in ZF-WT. Therefore, a water molecule could easily move towards the zinc ion to act as a fourth ligand, a common situation in catalytic zinc-binding sites of enzymes [45]. This water molecule could further stabilize zinc binding by forming a hydrogen bond (H-bond) to the backbone carbonyl oxygen of H22. Such a O(H22)···H_2O···Zn^{2+} configuration seems possible, since a O(H22)–Zn^{2+} distance of 4.5 ± 0.4 Å is found in the NMR ensemble, which is reasonable to accommodate a water molecule with

a correct H-bonding geometry. In 8 out of the 10 structures of the NMR ensemble refined in water, a water molecule is indeed found at this position (Figure 5), with distances O(H22)–Zn^{2+} of 4.5 ± 0.3 Å, O(H_2O)–Zn^{2+} of 2.2 ± 0.05 Å and O(H22)–H(H_2O) of 2.2 ± 0.5 Å. The entry of water molecules into the peptide core at initial stage of unfolding has been previously observed by molecular dynamics simulations [46], as well as the exchange of a zinc-chelating Cys for a water molecule in zinc fingers [47]. These studies suggested that zinc-bound water might be crucial for ZF folding by forming a stabilizing H-bond network to the polypeptide chain and allowing for local rearrangements. Finally, a biophysical characterization of several CCHX mutants (X = D, N, E, A) showed that the final chelating residue was not an essential feature of classical CCHH fingers to bind zinc and to form secondary structures in the presence of zinc. However, the global fold of the mutants seemed only partial and disordered as compared to the wild type [33]. In NEMO C417F mutant ZF, three zinc-chelating side chains are sufficient to induce a "native-like" folding and a water molecule stabilizing the coordination site might explain the native-like affinity of the mutant for zinc.

Structural and dynamical differences between the wild type and mutant zinc fingers

The averaged structures of ZF-C417F and ZF-WT are very similar in the non-flexible region encompassing the first to the third zinc-chelating residues F4-V23, with a pairwise RMSD of 0.32 Å and 0.74 Å on the backbone and heavy atoms, respectively. However, differences in dynamics and stability are clearly evident from homonuclear NMR data. Proton NMR chemical shifts at 25°C were used as very sensitive probes of variations in the local environment, in order to monitor subtle structural changes induced by the C/F point mutation in the structure. Since aromatic ring current contributions to proton shifts for ZF-WT and ZF-C417F were identical within the error bars (Supplementary Data Figure S3),

chemical shifts were not corrected for this effect. As expected, the largest differences ($\Delta\delta$) in H^N and H^α chemical shifts between ZF-WT and ZF-C417F are found around the zinc-binding site, spatially close to the C/F mutation, but significant differences are also observed in the entire β-hairpin and the C-terminal half of the α-helix (Supplementary Data Figure S4).

Enhanced instability of the b-hairpin in the C417F mutant. Chemical shifts of H-bonding protons have been reported as indicators for the strength of H-bonds [48], with high-frequency values (downfield) corresponding to short H-bond lengths. In the NMR ensemble of ZF-WT, the amide protons of F4, C6, Y11 and A13 pointing towards the interior of the β-hairpin are in H-bonded distances to the carbonyl oxygens of A13, Y11, C9 and F4, respectively. In addition, the amides of K8 and C9 may each participate in an amide-sulfur H-bond with the Sγ of C6, based on their respective nitrogen-sulfur distances (3.58 ± 0.23 Å and 3.77 ± 0.21 Å) and NH-S bond angles (133 ± 18° and 134 ± 7°). The downfield H^N chemical shifts observed for C6, K8, C9, Y11 and A13 in ZF-WT (Figure 2(a)) denote a tight H-bond network, which stabilizes the conformation of the β-sheet and the turn (Supplementary Data Figure S4(b)). However, in ZF-C417F, the H^N chemical shifts of C6, C9, Y11 and A13 move to significantly more upfield positions, as indicated by large positive $\Delta\delta(H^N)$ (Supplementary Data Figure S4(a)), while no changes are observed for the amides of C5, Q10 and Q12 pointing towards the solvent. In the absence of other factors that can influence proton chemical shifts (the C/F mutation is far away), this indicates that the β-hairpin H-bond network is significantly looser and/or more dynamic in the mutant than in the WT. Moreover, a strong typical inter-strand NOE is observed between H^α(C5) and H^α(Q12) in ZF-WT, together with a strong downfield shift of the H^α(C5) proton chemical shift (5.15 ppm), indicating that H^α(C5) might be involved in a weak C^α–H^α···O H-bond with the carbonyl oxygen acceptor of Y11. In ZF-C417F, a strong upfield shift is observed for H^α(C5)

(Supplementary Data Figure S4(a)), consistent with a weakening of this H^{α}-bond. Thus, the overall H-bond weakening in the F4-A13 region of the mutant can be attributed to a destabilization of this region and to an onset of β-hairpin opening. Finally, exchange rates of labile amide protons with water, as complementary information about H-bond stability and solvent accessibility, were qualitatively estimated by measuring the intensity attenuation in TOCSY spectra recorded with and without water resonance presaturation (data not shown). The increase in hydrogen exchange rates observed in the mutant, as indicated by larger attenuations, confirms the greater instability of the β-hairpin.

Premature end-fraying and increased dynamics of the α-helix in the C417F mutant. In the α-helix of ZF-WT, the chemical shifts of the solvent-exposed amide protons of I21, M24 and E25 are upfield shifted, whereas they are rather downfield shifted for V23 and to a lesser extent Q20, which both point toward the finger core (*Inset* of Supplementary Data Figure S4(a), filled circles). In the ZF-C417F peptide, the more uniform distribution of amide proton chemical shifts observed in the C-terminal half of the helix, with values gradually closer to random coil conformation (~ 8.2 ppm, *Inset* of Supplementary Data Figure S4(a), open circles) denotes a progressive reduction in α-helical propensity towards the C-terminus. In addition, conversely to ZF-WT, no α-helical NOE connectivities could be detected beyond M24, indicating that the helix ends shortly after the last chelating residue H22, and is therefore shorter than in ZF-WT by about one helical turn. This early end-fraying of the helix, as observed in the NMR ensemble (Figure 5), is due to the lack of the fourth zinc-chelating residue which holds the helix C-terminus to the coordination site via a strong Sγ(C26)-Zn bond.

Destabilization of the polar/acidic and hydrophobic surfaces induced by the C417F mutation. In the mutant, the fraying of the α-helix C-terminus and the subsequent high flexibility beyond H22 strongly affect the packing and stability of the side chains on both

potential protein-binding surfaces. Indeed, the high disorder of the acidic residue E25 and of F26 destabilizes the edge of the polar/acidic surface (Supplementary Data Figure S2(a)). On the opposite face, about half of the hydrophobic surface is largely disordered (i.e. residues V23, M24 and I27 on Supplementary Data Figure S2(b)). Therefore, the overall instability and increased dynamics observed in the secondary structures of the C417F mutant may be sufficient to impair its protein-recognition properties.

Thermal stability of the wild type and C417F mutant zinc-fingers

To further compare the stability of ZF-WT and ZF-C417F, we recorded far-UV CD spectra and monitored temperature-induced unfolding of both peptides (Figure 6). The ZF-C417F spectrum markedly differs from that of ZF-WT (Figure 6, *Inset*). Deconvolution of the CD spectra revealed a decrease in helical content from ~27 % for ZF-WT to ~19 % for ZF-C417F, consistent with the shortening of the mutant α-helix by about one turn deduced from NMR data (see above). Thermal denaturations of both peptides were performed by measuring the far-UV CD ellipticity at 222 nm from 1°C to 95°C. For ZF-WT, a complete temperature-induced unfolding transition could not be observed in the temperature range studied (Figure 6, filled circles). The melting temperature (T_m) is above 90°C, indicating that the WT peptide is very thermostable, as commonly observed for classical zinc fingers. In contrast, the melting curve for ZF-C417F describes a complete two-state transition, with a midpoint at 48.8 ± 0.4 °C and a cooperativity of 4.8 ± 0.2 (Figure 6, open circles), indicating that the mutant ZF is significantly less stable than the WT. In conclusion, our analysis of NMR and CD data provides strong evidence for substantial instability in the secondary structures of the mutant.

The slight decrease in the CD signal absolute value of ZF-WT between 35°C and 27°C (Figure 6, filled circles), together with a blue shift of the minimum at 206 nm by about 1 nm (not shown), could be attributed to a partial cold denaturation. Since a similar behavior

was observed with the PPP-ZF-WT construct mentioned previously (data not shown), we assume that this effect is not due to experimental artifacts. Cold denaturation is usually attributed to a weakening of the hydrophobic forces at low temperature [49], but is rarely observed at temperatures above zero under physiological conditions. Although essentially maintained by zinc coordination, the structure of NEMO ZF is also highly dependent on hydrophobic interactions to ensure proper packing of the core. A weakening of hydrophobic forces at low temperature could destabilize to some extent the packing of the core and lead to the observed partial cold denaturation.

Incidence of the pathogenic C417F mutation on the NF-kB pathway activation

Considering the instability of the mutant peptide revealed by the NMR and CD experiments, we first assessed the expression level of the full-length pathogenic protein in cells. Transient transfections of 293T cells revealed that it was expressed at a similar level than the wild type protein (Figure 7(a)). We next compared the activation of the NF-κB pathway mediated by the WT and pathogenic proteins by transfections of NEMO-deficient cells. Pre-B (1.3E2 [3]) and T (JM4.5.2 [50]) lymphocytes were transiently co-transfected with the WT or the C417F mutant *NEMO*, together with a NF-κB reporter construct. Pre-B cells lacking TNF-α receptor 1 were subsequently stimulated with LPS or IL-1β whereas T cells were activated with TNF-α. As shown in Figure 7(b), the pathogenic protein did not completely restore the NF-κB activation in response to these stimuli, displaying 75%, 34% and 25% of activity compared to the WT protein in response to LPS, IL-1β and TNFα, respectively. These differences were reproducible and are consistent with the fact that NEMO hypomorphic mutations like EDA-ID C417F do not totally suppress the activation of the NF-κB pathway. Indeed, an activation level of 75-80% has been shown to be sufficient to cause

the EDA-ID phenotype in case of other mutations [26]. Two EDA-ID patients carrying the C417F mutation have been described so far [9, 11]. Both patients presented a susceptibility to infections by Gram-negative and -positive bacteria, in particular *S. pneumoniae*, and presented all the developmental signs associated with EDA. The alteration of the NF-κB pathway that we observed in response to endotoxins and pro-inflammatory cytokines is highly consistent with the defect in innate immunity described in patients and responsible for recurrent infections. Moreover, several studies have previously shown in different cell types that NEMO ZF was required for a full NF-κB activation in response to LPS, IL-1β and TNF-α [27, 32, 51]. In particular Schwamborn et *al.*, in the same experiment as we performed here, showed that NEMO deleted of its ZF motif only partially complements the 1.3E2 cell line in response to LPS, displaying 30% of NF-κB activation compared to the full-length protein. The C417F mutant NEMO restores the NF-κB activation level by 75%, indicating that the mutant ZF, despite its large instability and flexibility revealed by our study, is still able to act as a functional motif in the LPS-induced NF-κB pathway. Interestingly, although the activation cascade upstream of NEMO and leading to NF-κB activation is thought to be shared by LPS and IL-1β, we find that the IL-1β pathway is significantly more affected by the C417F mutation. This suggests that one or several proteins may be specific for this pathway, and that their interaction with NEMO is more specifically altered by the ZF instability.

Conclusion

We have presented a detailed analysis of the structural and functional properties of the CCHC ZF motif of NEMO and of the EDA-ID-related C417F pathogenic mutant. The WT ZF binds a single zinc ion with a modest affinity and adopts a ββα structure highly similar to

that of classical fingers. In spite of a missing chelating residue, zinc-affinity is not significantly affected by the Cys/Phe mutation and the mutant average structure closely resembles that of the WT, with a water molecule likely acting as the fourth zinc-ligand. However, a strong decrease in thermal stability is observed for the mutant, as well as marked dynamic instability, as revealed by an overall looser H-bond network and a premature α-helix end-fraying beyond the third chelating residue. Based on a number of observations, we could delineate two possible non-overlapping protein-binding surfaces in NEMO ZF. The first one, on the polar/acidic face of the finger, encompasses the typical DNA-binding interface of classical zinc fingers and overlaps to some extent with a few protein-binding regions reported so far. The second one is mostly defined by hydrophobic residues lying on the opposite face of the α-helix. In the C417F mutant, a large destabilization of the two surfaces is induced by the early helix fraying from H22, which may impair its protein-recognition abilities. Moreover, functional complementation assays using NEMO-deficient pre-B and T lymphocytes showed that full-length C417F NEMO leads to a partial to strong defect of LPS, IL-1β and TNF-α-induced NF-κB activation, respectively, as compared to WT NEMO, consistent with inhibition levels induced by NEMO hypomorphic mutations leading to EDA-ID. Our results suggest that the functional defect induced by the C417F mutation is neither due to a defect in Zn^{2+} affinity nor to an incapacity to fold, but rather to a change in the finger dynamics and stability that might have consequences for its mechanism of protein-recognition. This further demonstrates how much the structural integrity of NEMO zinc finger is crucial to the function of the protein, though its actual role remains to be unraveled. Finally, while studying the function of zinc finger motifs, one should be careful when using point mutations of zinc chelating residues under the assumption that these mutations will destroy the structure of the motif and abrogate its function. Indeed, in the light of our study, the structure of such a mutant can still be largely preserved.

We propose candidates for the protein-protein interactions mediated by NEMO ZF via its two distinct faces. Firstly, the observation by fluorescence spectroscopy of a tyrosinate (Y11) signal in the CC2-LZ-ZF domain and its absence in the isolated ZF suggest that the protein-binding surface defined by the acidic face of the finger likely interacts with the CC2-LZ coiled-coil domain, rich in basic residues. Secondly, binding of NEMO CC2-LZ domain to K63-polyubiquitin chains, in particular the ones formed on RIP1 in response to TNF-α, has been recently shown to be important for IKK activation, although the ZF motif seems dispensable for polyubiquitin binding [24, 25]. Surprisingly, a careful analysis of the ZF sequence and atomic structure reveals that the α-helix hydrophobic side shares similarities with the ubiquitin interacting region of the ubiquitin-binding zinc finger (UBZ) domain of human DNA Y-polymerase (pol) η [52]. Key residues essential for binding are indeed well conserved between NEMO ZF and pol η UBZ, as well as inverted ubiquitin-interacting motifs (IUIM [53]). These observations lead us to hypothesize that NEMO ZF could actually serve as a ubiquitin-recognition motif in conjunction with the CC2-LZ domain, and experiments are in progress to validate this hypothesis.

Materials and Methods

Sample preparation

The two synthetic peptides (ZF-WT and ZF-C417F) with greater than 98% purity (after reverse-phase HPLC purification) were purchased from Biopeptide Co. (San Diego, USA) and are termini-blocked by N-acetyl and C-amide groups. Electrospray mass spectrometry and amino acid analysis showed correct mass, purity and amino acid

composition of the peptides. Sequences of the WT and mutant peptides are described in Figure 1(b).

NMR samples (Shigemi NMR microtubes) were prepared by dissolving 1.3 mg of lyophilized ZF-WT or ZF-C417F, in 400 µl of a 2 mM $ZnSO_4$, 2 mM TCEP, 90% H_2O/10% D_2O buffer. The pH of these solutions (in the range 2-3) was adjusted to 7.3 for ZF-WT and to 6.6 for ZF-C417F by addition of 0.1 M NaOH. Final concentration of each peptide:$ZnSO_4$ sample was ~ 1:2 mM and was verified by amino acid analysis. Samples of apo-peptides were prepared by dissolving 0.75 mg of either ZF-WT or ZF-C417F in 300 µl of buffer containing 2 mM TCEP, 20 mM sodium phosphate, 90% H_2O/10% D_2O. The pH was adjusted to 6.9 and the concentration of each apo-peptide was ~ 0.75 mM.

NMR spectroscopy

Standard 2D homonuclear ^1H experiments were carried out on a Varian Inova 600 MHz spectrometer equipped with a cryoprobe. TOCSY (mixing times τ_m = 70 and 100 ms), NOESY (τ_m = 150 and 220 ms) and purged-COSY experiments for proton assignment and ^1H-^1H NOE and $^3J_{HNH\alpha}$ scalar coupling restraints were acquired, as previously described [54], on the two samples of ZF-WT and ZF-C417F in presence of $ZnSO_4$. Experiments were recorded at 25 and 40°C for ZF-WT and at 15 and 25°C for ZF-C417F, since resonance broadening was observed for the latter at higher temperatures due to its thermal instability (see text). Experiments were also recorded at 25°C on apo-ZF-WT and apo-ZF-C417F samples. Spectra were processed using the NMRPipe software package [55] and analyzed with NMRView 5.03 [56]. Chemical shifts were referenced relative to the sodium salt of 4,4-dimethyl-4-silapentane sulfonate. Proton resonance assignments were achieved by the standard homonuclear method [57].

Structure Calculation

Structures of ZF-WT were calculated with the program ARIA1.2 (Ambiguous Restraints for Interactive Assignment) [58] as an extension of CNS 1.1 [59], from NMR data obtained at 25°C (NOESY (mixing time, 220 ms) and $^{3}J_{HNH\alpha}$ scalar couplings). From initial calculations performed without zinc ion, it was evident that the zinc coordination site was defined by the three thiol groups of C6, C9 and C26 and by the $N^{\varepsilon 2}$ atom of H22. As a single Zn^{2+} site was identified in this finger by flame atomic absorption spectroscopy, a zinc ion was included in the subsequent and final calculations, assuming a tetrahedral geometry of the zinc coordination (Zn-S^{γ}, Zn-$N^{\varepsilon 2}$, S^{γ}-S^{γ} and S^{γ}-$N^{\varepsilon 2}$ bond lengths were set to 2.3, 2.0, 3.7 and 3.5 Å, respectively). Of the 200 computed structures, the 80 conformers with the lower total energy were refined in an explicit water box [60]. Finally, the 10 refined conformers of lowest energy were selected to represent the final NMR ensemble and were analyzed with PROCHECK 3.54 [61]. Structures of ZF-C417F were calculated from data obtained at 25°C, following the same protocol as described for ZF-WT, except that the zinc coordination was defined by the two thiol groups of C6 and C9 and by the $N^{\varepsilon 2}$ atom of H22. We ensured that D15, D17, Q20, E25 and E28 could not act as the fourth ligand (see text). More details on structure calculations are given in the Supplementary Data. For the WT and the mutant, no NOE violations greater than 0.25 Å or dihedral angle violation greater than 5° were observed. The statistics of the ensembles and of the experimental restraints are given in Supplementary Data Table S1. Figures of the structures were generated using the MolMol program [62].

Far-UV CD spectroscopy

Far-UV CD measurements were performed on an Aviv 215 spectropolarimeter (Aviv Instruments, Lakewood, NJ) equipped with Peltier temperature controller, using a 1-mm path length cell. CD spectra were recorded at 1°C on ZF-WT and ZF-C417F samples at

concentrations (verified by amino acid analysis) of 21 and 41 μM, respectively, in a buffer containing 2 mM TCEP, 10 mM sodium phosphate, pH 7.3 and a 1.5 fold excess of $ZnSO_4$, and with experimental setup as described in [26]. Spectra were baseline corrected. Secondary structure prediction was achieved using the program CDsstr [63]. Thermal denaturation experiments were performed on samples of ZF-WT and ZF-C417F at concentrations of 75 μM, by measuring the ellipticity at 222 nm from 1 to 95°C in 1°C steps, at a rate of 1°C/min, with a 2 nm bandwidth. Temperature equilibration time was set to 0.1 min and temperature dead band to 0.1°C. An averaging time of 2 s was used. The ellipticity, baseline corrected with respect to the buffer signal at 20°C, was converted to differential extinction coefficient $\Delta\varepsilon$ (M^{-1} cm^{-1}) per residue. For ZF-C417F, non-linear least square fitting of the melting curve to standard equation describing a two-state transition was achieved to estimate the melting temperature and the cooperativity, as described in [26].

Zinc titration by fluorescence spectroscopy

Fluorescence measurements were carried out with a PTI QuantaMaster spectrofluorimeter (PTI, Lawrenceville, NJ) equipped with a thermostated cuvette holder. All experiments were performed in a 1-cm path length quartz cuvette of 1 ml allowing permanent stirring, with bandwidths of excitation and emission monochromators set to 3 and 6 nm, respectively. Fluorescence emission spectra were recorded on ZF-WT at 1 μM, 25°C in the absence or in the presence of a saturating amount of Zn^{2+} (10 μM $ZnSO_4$). The equilibrium Zn^{2+}-binding constants were determined by zinc titrations at 25°C and 37°C. Aliquots of solutions containing 10-1000 μM $ZnSO_4$ (pH 7.3) were added to solutions of ZF-WT or ZF-C417F at 1 μM, each dissolved in PBS buffer, pH 7.3 containing 50 μM TCEP. Excitation wavelength was set to 285 nm in order to minimize the contribution of the phenylalanines. Fluorescence emission of Y11 at 307 nm was measured at each point of the titration, allowing

for equilibration after each Zn^{2+} addition for the time required (~ 2 min). Each point was obtained from an average of 300 scans. Following fluorescence titrations, the fraction of zinc-bound peptide was calculated as $(F_{obs}-F_0)/(F_{max}-F_0)$, where F_{obs} is the observed fluorescence, F_0 the initial fluorescence before addition of Zn^{2+} and F_{max} the fluorescence after saturation with Zn^{2+}. Non-linear least square fitting of the data was achieved using the quadratic binding equation:

$$(F_{obs}-F_0)/(F_{max}-F_0)=\left(K_D+n\cdot ZF_T+Zn_T^{2+}-\sqrt{\left(K_D+n\cdot ZF_T+Zn_T^{2+}\right)^2-4\cdot n\cdot ZF_T\cdot Zn_T^{2+}}\right)\Big/(2\cdot n\cdot ZF_T)$$

where K_D is the dissociation constant, ZF_T the total peptide concentration, n the stoichiometry and Zn_T^{2+} the total Zn^{2+} concentration.

Flame atomic absorption spectroscopy

Samples of the WT and mutant ZF peptides at 5 µM were prepared in a sodium phosphate buffer (30 mM, pH 7.3) containing 30 µM TCEP and 15 µM $ZnSO_4$. Samples were dialyzed overnight in the sodium phosphate/TCEP buffer in order to remove excess of Zn^{2+}. Measurements were performed as previously described [64]. Briefly, the molar amounts of the WT and mutant ZF peptides (100 µl at 1-5 µM) were measured at 213.9 nm using a flame atomic absorption spectrophotometer (type Varian SpectrAA220). The zinc content of ZF peptide was evaluated from a standard curve obtained with $ZnSO_4$ in the above buffer at different concentrations in the range 0-10 µM.

Cell lines and transient transfections

Human NEMO cDNA (*hNEMO*) was inserted into a pcDNA3 vector as described previously [65]. A G→T missense mutation at nucleotide 1,250 was identified in two patients with EDA-ID [9, 11], resulting in a Cys→Phe replacement at position 417 within the ZF motif of hNEMO. The same nucleotide mutation was introduced in the pcDNA3 construct by using

the QuikChange site-directed mutagenesis method (Stratagene) (primer sequences are available upon request). The nucleotide sequence was verified by DNA sequencing.

The 1.3E2 NEMO deficient murine pre-B cell line was maintained and transfected as described previously [3]. NEMO$^{-/-}$ Jurkat T cells (JM4.5.2, [50]) were grown in RPMI 1640 medium supplemented with 10% fetal calf serum and antibiotics. These cells were transiently transfected using a DEAE-Dextran method and subsequently activated with TNF-α as reported earlier [26]. 293T cells were transiently transfected using calcium phosphate-DNA precipitates formed in HEPES. After 24 h, cytoplasmic extracts were prepared as described previously [3] and analyzed with a polyclonal anti-NEMO antibody (FL-419, Santa Cruz Biotechnology).

Protein Data Bank accession number

The coordinates and structural restraints have been deposited in the Brookhaven Protein Data Bank under accession code **2jvx** for ZF-WT and **2jvy** for ZF-C417F.

Acknowledgements

We thank Iñaki Guijarro, Robert Weil and Alain Israël for valuable discussions, Michael Nilges for help with Aria, Alain Chaffotte and Patrick England for advices with CD measurements, Sylviane Hoos for help with isothermal titration calorimetry, Myriam Lazard for flame atomic absorption spectroscopy experiments, Pascal Lenormand for mass spectrometry analysis and Olivera Grubisha for critical reading of the manuscript. E.V. is recipient of a fellowship from the Ministère de l'Enseignement Supérieur et de la Recherche (MESR). This work was supported in part by grants from the Association pour la Recherche sur le Cancer, the Cancéropôle Ile-de-France and the BNP-Paribas Foundation.

Supplementary Data

Supplementary data associated with this article can be found, in the online version, at XXXXX.

References

1. Hayden, M. S. & Ghosh, S. (2004). Signaling to NF-kappaB. *Genes Dev* **18**, 2195-224.
2. Fontan, E., Traincard, F., Levy, S. G., Yamaoka, S., Veron, M. & Agou, F. (2007). NEMO oligomerization in the dynamic assembly of the IkappaB kinase core complex. *Febs J* **274**, 2540-51.
3. Yamaoka, S., Courtois, G., Bessia, C., Whiteside, S. T., Weil, R., Agou, F., Kirk, H. E., Kay, R. J. & Israel, A. (1998). Complementation cloning of NEMO, a component of the IkappaB kinase complex essential for NF-kappaB activation. *Cell* **93**, 1231-1240.
4. Rudolph, D., Yeh, W. C., Wakeham, A., Rudolph, B., Nallainathan, D., Potter, J., Elia, A. J. & Mak, T. W. (2000). Severe liver degeneration and lack of NF-kappaB activation in NEMO/IKKgamma-deficient mice. *Genes Dev* **14**, 854-62.
5. Zhao, T., Yang, L., Sun, Q., Arguello, M., Ballard, D. W., Hiscott, J. & Lin, R. (2007). The NEMO adaptor bridges the nuclear factor-kappaB and interferon regulatory factor signaling pathways. *Nat Immunol* **8**, 592-600.
6. Courtois, G. & Smahi, A. (2006). NF-kappaB-related genetic diseases. *Cell Death Differ* **13**, 843-51.
7. Smahi, A., Courtois, G., Vabres, P., Yamaoka, S., Heuertz, S., Munnich, A., Israel, A., Heiss, N. S., Klauck, S. M., Kioschis, P., Wiemann, S., Poustka, A., Esposito, T., Bardaro, T., Gianfrancesco, F., Ciccodicola, A., D'Urso, M., Woffendin, H., Jakins, T., Donnai, D., Stewart, H., Kenwrick, S. J., Aradhya, S., Yamagata, T., Levy, M., Lewis, R. A. & Nelson, D. L. (2000). Genomic rearrangement in NEMO impairs NF-kappaB activation and is a cause of incontinentia pigmenti. The International Incontinentia Pigmenti (IP) Consortium. *Nature* **405**, 466-72.
8. Aradhya, S., Woffendin, H., Jakins, T., Bardaro, T., Esposito, T., Smahi, A., Shaw, C., Levy, M., Munnich, A., D'Urso, M., Lewis, R. A., Kenwrick, S. & Nelson, D. L. (2001). A recurrent deletion in the ubiquitously expressed NEMO (IKK-gamma) gene accounts for the vast majority of incontinentia pigmenti mutations. *Hum Mol Genet* **10**, 2171-9.
9. Doffinger, R., Smahi, A., Bessia, C., Geissmann, F., Feinberg, J., Durandy, A., Bodemer, C., Kenwrick, S., Dupuis-Girod, S., Blanche, S., Wood, P., Rabia, S. H., Headon, D. J., Overbeek, P. A., Le Deist, F., Holland, S. M., Belani, K., Kumararatne, D. S., Fischer, A., Shapiro, R., Conley, M. E., Reimund, E., Kalhoff, H., Abinun, M., Munnich, A., Israel, A., Courtois, G. & Casanova, J. L. (2001). X-linked anhidrotic ectodermal dysplasia with immunodeficiency is caused by impaired NF-kappaB signaling. *Nat Genet* **27**, 277-85.
10. Jain, A., Ma, C. A., Liu, S., Brown, M., Cohen, J. & Strober, W. (2001). Specific missense mutations in NEMO result in hyper-IgM syndrome with hypohydrotic ectodermal dysplasia. *Nat Immunol* **2**, 223-8.
11. Zonana, J., Elder, M. E., Schneider, L. C., Orlow, S. J., Moss, C., Golabi, M., Shapira, S. K., Farndon, P. A., Wara, D. W., Emmal, S. A. & Ferguson, B. M. (2000). A novel X-linked disorder of immune deficiency and hypohidrotic ectodermal dysplasia is allelic

to incontinentia pigmenti and due to mutations in IKK-gamma (NEMO). *Am J Hum Genet* **67**, 1555-62.

12. Ku, C. L., Dupuis-Girod, S., Dittrich, A. M., Bustamante, J., Santos, O. F., Schulze, I., Bertrand, Y., Couly, G., Bodemer, C., Bossuyt, X., Picard, C. & Casanova, J. L. (2005). NEMO mutations in 2 unrelated boys with severe infections and conical teeth. *Pediatrics* **115**, e615-9.
13. Niehues, T., Reichenbach, J., Neubert, J., Gudowius, S., Puel, A., Horneff, G., Lainka, E., Dirksen, U., Schroten, H., Doffinger, R., Casanova, J. L. & Wahn, V. (2004). Nuclear factor kappaB essential modulator-deficient child with immunodeficiency yet without anhidrotic ectodermal dysplasia. *J Allergy Clin Immunol* **114**, 1456-62.
14. Orange, J. S., Levy, O., Brodeur, S. R., Krzewski, K., Roy, R. M., Niemela, J. E., Fleisher, T. A., Bonilla, F. A. & Geha, R. S. (2004). Human nuclear factor kappa B essential modulator mutation can result in immunodeficiency without ectodermal dysplasia. *J Allergy Clin Immunol* **114**, 650-6.
15. Filipe-Santos, O., Bustamante, J., Haverkamp, M. H., Vinolo, E., Ku, C. L., Puel, A., Frucht, D. M., Christel, K., von Bernuth, H., Jouanguy, E., Feinberg, J., Durandy, A., Senechal, B., Chapgier, A., Vogt, G., de Beaucoudrey, L., Fieschi, C., Picard, C., Garfa, M., Chemli, J., Bejaoui, M., Tsolia, M. N., Kutukculer, N., Plebani, A., Notarangelo, L., Bodemer, C., Geissmann, F., Israel, A., Veron, M., Knackstedt, M., Barbouche, R., Abel, L., Magdorf, K., Gendrel, D., Agou, F., Holland, S. M. & Casanova, J. L. (2006). X-linked susceptibility to mycobacteria is caused by mutations in NEMO impairing CD40-dependent IL-12 production. *J Exp Med* **203**, 1745-59.
16. Rothwarf, D. M., Zandi, E., Natoli, G. & Karin, M. (1998). IKK-gamma is an essential regulatory subunit of the IkappaB kinase complex. *Nature* **395**, 297-300.
17. Agou, F., Ye, F., Goffinont, S., Courtois, G., Yamaoka, S., Israel, A. & Veron, M. (2002). NEMO trimerizes through its coiled-coil C-terminal domain. *J Biol Chem* **277**, 17464-75.
18. Poyet, J.-L., Srinivasula, S. M., Lin, J.-H., Fernandes-Alnemri, T., Yamaoka, S., Tsichlis, P. N. & Alnemri, E. S. (2000). Activation of the IkB kinases by RIP via IKKγ/NEMO-mediated oligomerization. *Journal of Biological Chemistry* **275**, 37966-37977.
19. Agou, F., Traincard, F., Vinolo, E., Courtois, G., Yamaoka, S., Israel, A. & Veron, M. (2004). The trimerization domain of NEMO is composed of the interacting C-terminal CC2 and LZ coiled-coil subdomains. *J Biol Chem* **279**, 27861-9.
20. Carter, R. S., Pennington, K. N., Ungurait, B. J. & Ballard, D. W. (2003). In vivo identification of inducible phosphoacceptors in the IKKgamma/NEMO subunit of human IkappaB kinase. *J Biol Chem* **278**, 19642-8.
21. Prajapati, S. & Gaynor, R. B. (2002). Regulation of Ikappa B kinase (IKK)gamma /NEMO function by IKKbeta -mediated phosphorylation. *J Biol Chem* **277**, 24331-9.
22. Tang, E. D., Wang, C. Y., Xiong, Y. & Guan, K. L. (2003). A role for NF-kappaB essential modifier/IkappaB kinase-gamma (NEMO/IKKgamma) ubiquitination in the activation of the IkappaB kinase complex by tumor necrosis factor-alpha. *J Biol Chem* **278**, 37297-305.
23. Zhou, H., Wertz, I., O'Rourke, K., Ultsch, M., Seshagiri, S., Eby, M., Xiao, W. & Dixit, V. M. (2004). Bcl10 activates the NF-kappaB pathway through ubiquitination of NEMO. *Nature* **427**, 167-71.
24. Ea, C. K., Deng, L., Xia, Z. P., Pineda, G. & Chen, Z. J. (2006). Activation of IKK by TNFalpha requires site-specific ubiquitination of RIP1 and polyubiquitin binding by NEMO. *Mol Cell* **22**, 245-57.

25. Wu, C. J., Conze, D. B., Li, T., Srinivasula, S. M. & Ashwell, J. D. (2006). NEMO is a sensor of Lys 63-linked polyubiquitination and functions in NF-kappaB activation. *Nat Cell Biol* **8**, 398-406.
26. Vinolo, E., Sebban, H., Chaffotte, A., Israel, A., Courtois, G., Veron, M. & Agou, F. (2006). A Point Mutation in NEMO Associated with Anhidrotic Ectodermal Dysplasia with Immunodeficiency Pathology Results in Destabilization of the Oligomer and Reduces Lipopolysaccharide- and Tumor Necrosis Factor-mediated NF-{kappa}B Activation. *J Biol Chem* **281**, 6334-48.
27. Makris, C., Roberts, J. L. & Karin, M. (2002). The carboxyl-terminal region of IkappaB kinase gamma (IKKgamma) is required for full IKK activation. *Mol Cell Biol* **22**, 6573-81.
28. Huang, T. T., Feinberg, S. L., Suryanarayanan, S. & Miyamoto, S. (2002). The zinc finger domain of NEMO is selectively required for NF-kappa B activation by UV radiation and topoisomerase inhibitors. *Mol Cell Biol* **22**, 5813-25.
29. Shambharkar, P. B., Blonska, M., Pappu, B. P., Li, H., You, Y., Sakurai, H., Darnay, B. G., Hara, H., Penninger, J. & Lin, X. (2007). Phosphorylation and ubiquitination of the IkappaB kinase complex by two distinct signaling pathways. *Embo J* **26**, 1794-805.
30. Liew, C. K., Kowalski, K., Fox, A. H., Newton, A., Sharpe, B. K., Crossley, M. & Mackay, J. P. (2000). Solution structures of two CCHC zinc fingers from the FOG family protein U-shaped that mediate protein-protein interactions. *Structure Fold Des* **8**, 1157-66.
31. Jain, A., Ma, C. A., Lopez-Granados, E., Means, G., Brady, W., Orange, J. S., Liu, S., Holland, S. & Derry, J. M. (2004). Specific NEMO mutations impair CD40-mediated c-Rel activation and B cell terminal differentiation. *J Clin Invest* **114**, 1593-602.
32. Yang, F., Yamashita, J., Tang, E., Wang, H. L., Guan, K. & Wang, C. Y. (2004). The zinc finger mutation C417R of I-kappa B kinase gamma impairs lipopolysaccharide- and TNF-mediated NF-kappa B activation through inhibiting phosphorylation of the I-kappa B kinase beta activation loop. *J Immunol* **172**, 2446-52.
33. Simpson, R. J., Cram, E. D., Czolij, R., Matthews, J. M., Crossley, M. & Mackay, J. P. (2003). CCHX zinc finger derivatives retain the ability to bind Zn(II) and mediate protein-DNA interactions. *J Biol Chem* **278**, 28011-8.
34. Berg, J. M. & Godwin, H. A. (1997). Lessons from zinc-binding peptides. *Annu Rev Biophys Biomol Struct* **26**, 357-71.
35. Walkup, G. & Imperiali, B. (1996). Design and Evaluation of a Peptidyl Fluorescent Chemosensor for Divalent Zinc. *Journal of the American Chemical Society* **118**, 3053-3054.
36. Hutchinson, E. G. & Thornton, J. M. (1996). PROMOTIF--a program to identify and analyze structural motifs in proteins. *Protein Sci* **5**, 212-20.
37. Kochoyan, M., Havel, T. F., Nguyen, D. T., Dahl, C. E., Keutmann, H. T. & Weiss, M. A. (1991). Alternating zinc fingers in the human male associated protein ZFY: 2D NMR structure of an even finger and implications for "jumping-linker" DNA recognition. *Biochemistry* **30**, 3371-86.
38. Kochoyan, M., Keutmann, H. T. & Weiss, M. A. (1991). Alternating zinc fingers in the human male associated protein ZFY: refinement of the NMR structure of an even finger by selective deuterium labeling and implications for DNA recognition. *Biochemistry* **30**, 7063-72.
39. Lachenmann, M. J., Ladbury, J. E., Phillips, N. B., Narayana, N., Qian, X. & Weiss, M. A. (2002). The hidden thermodynamics of a zinc finger. *J Mol Biol* **316**, 969-89.
40. Liew, C. K., Simpson, R. J., Kwan, A. H., Crofts, L. A., Loughlin, F. E., Matthews, J. M., Crossley, M. & Mackay, J. P. (2005). Zinc fingers as protein recognition motifs:

structural basis for the GATA-1/friend of GATA interaction. *Proc Natl Acad Sci U S A* **102**, 583-8.
41. Wolfe, S. A., Nekludova, L. & Pabo, C. O. (2000). DNA recognition by Cys2His2 zinc finger proteins. *Annu Rev Biophys Biomol Struct* **29**, 183-212.
42. Gamsjaeger, R., Liew, C. K., Loughlin, F. E., Crossley, M. & Mackay, J. P. (2007). Sticky fingers: zinc-fingers as protein-recognition motifs. *Trends Biochem Sci* **32**, 63-70.
43. Simpson, R. J., Yi Lee, S. H., Bartle, N., Sum, E. Y., Visvader, J. E., Matthews, J. M., Mackay, J. P. & Crossley, M. (2004). A classic zinc finger from friend of GATA mediates an interaction with the coiled-coil of transforming acidic coiled-coil 3. *J Biol Chem* **279**, 39789-97.
44. Dawid, I. B., Breen, J. J. & Toyama, R. (1998). LIM domains: multiple roles as adapters and functional modifiers in protein interactions. *Trends Genet* **14**, 156-62.
45. Sankaranarayanan, R., Dock-Bregeon, A. C., Romby, P., Caillet, J., Springer, M., Rees, B., Ehresmann, C., Ehresmann, B. & Moras, D. (1999). The structure of threonyl-tRNA synthetase-tRNA(Thr) complex enlightens its repressor activity and reveals an essential zinc ion in the active site. *Cell* **97**, 371-81.
46. Caflisch, A. & Karplus, M. (1994). Molecular dynamics simulation of protein denaturation: solvation of the hydrophobic cores and secondary structure of barnase. *Proc Natl Acad Sci U S A* **91**, 1746-50.
47. Bredenberg, J. & Nilsson, L. (2002). Conformational states of the glucocorticoid receptor DNA-binding domain from molecular dynamics simulations. *Proteins* **49**, 24-36.
48. Wagner, G., Pardi, a. & Wuthrich, K. (1983). Hydrogen-Bond Length and H-1-Nmr Chemical-Shifts in Proteins. *Journal of the American Chemical Society* **105**, 5948-5949.
49. Privalov, P. L. (1990). Cold denaturation of proteins. *Crit Rev Biochem Mol Biol* **25**, 281-305.
50. Harhaj, E. W., Good, L., Xiao, G., Uhlik, M., Cvijic, M. E., Rivera-Walsh, I. & Sun, S. C. (2000). Somatic mutagenesis studies of NF-kappa B signaling in human T cells: evidence for an essential role of IKK gamma in NF-kappa B activation by T-cell costimulatory signals and HTLV-I Tax protein. *Oncogene* **19**, 1448-56.
51. Schwamborn, K., Weil, R., Courtois, G., Whiteside, S. T. & Israel, A. (2000). Phorbol esters and cytokines regulate the expression of the NEMO-related protein, a molecule involved in a NF-kappa B-independent pathway. *Journal of Biological Chemistry* **275**, 22780-22789.
52. Bomar, M. G., Pai, M. T., Tzeng, S. R., Li, S. S. & Zhou, P. (2007). Structure of the ubiquitin-binding zinc finger domain of human DNA Y-polymerase eta. *EMBO Rep* **8**, 247-51.
53. Lee, S., Tsai, Y. C., Mattera, R., Smith, W. J., Kostelansky, M. S., Weissman, A. M., Bonifacino, J. S. & Hurley, J. H. (2006). Structural basis for ubiquitin recognition and autoubiquitination by Rabex-5. *Nat Struct Mol Biol* **13**, 264-71.
54. Guijarro, J. I., M'Barek, S., Gomez-Lagunas, F., Garnier, D., Rochat, H., Sabatier, J. M., Possani, L. & Delepierre, M. (2003). Solution structure of Pi4, a short four-disulfide-bridged scorpion toxin specific of potassium channels. *Protein Sci* **12**, 1844-54.
55. Delaglio, F., Grzesiek, S., Vuister, G. W., Zhu, G., Pfeifer, J. & Bax, A. (1995). NMRPipe: a multidimensional spectral processing system based on UNIX pipes. *J Biomol NMR* **6**, 277-93.
56. Johnson, B. a. & Blevins, R. a. (1994). Nmr View - a Computer-Program for the Visualization and Analysis of Nmr Data. *Journal of Biomolecular Nmr* **4**, 603-614.

57. Wüthrich, K. (1986). *NMR of Proteins and Nucleic Acids*, John Wiley & Sons, New York.
58. Linge, J. P., O'Donoghue, S. I. & Nilges, M. (2001). Automated assignment of ambiguous nuclear overhauser effects with ARIA. *Nuclear Magnetic Resonance of Biological Macromolecules, Pt B* **339**, 71-90.
59. Brunger, a. T., Adams, P. D., Clore, G. M., DeLano, W. L., Gros, P., Grosse-Kunstleve, R. W., Jiang, J. S., Kuszewski, J., Nilges, M., Pannu, N. S., Read, R. J., Rice, L. M., Simonson, T. & Warren, G. L. (1998). Crystallography & NMR system: A new software suite for macromolecular structure determination. *Acta Crystallographica Section D-Biological Crystallography* **54**, 905-921.
60. Linge, J. P., Williams, M. A., Spronk, C. A. E. M., Bonvin, A. M. J. J. & Nilges, M. (2003). Refinement of protein structures in explicit solvent. *Proteins-Structure Function and Genetics* **50**, 496-506.
61. Laskowski, R. a., Macarthur, M. W., Moss, D. S. & Thornton, J. M. (1993). Procheck - a Program to Check the Stereochemical Quality of Protein Structures. *Journal of Applied Crystallography* **26**, 283-291.
62. Koradi, R., Billeter, M. & Wuthrich, K. (1996). MOLMOL: A program for display and analysis of macromolecular structures. *Journal of Molecular Graphics* **14**, 51-55.
63. Johnson, W. C. (1999). Analyzing protein circular dichroism spectra for accurate secondary structures. *Proteins* **35**, 307-12.
64. Ferri-Fioni, M. L., Schmitt, E., Soutourina, J., Plateau, P., Mechulam, Y. & Blanquet, S. (2001). Structure of crystalline D-Tyr-tRNA(Tyr) deacylase. A representative of a new class of tRNA-dependent hydrolases. *J Biol Chem* **276**, 47285-90.
65. Fusco, F., Bardaro, T., Fimiani, G., Mercadante, V., Miano, M. G., Falco, G., Israel, A., Courtois, G., D'Urso, M. & Ursini, M. V. (2004). Molecular analysis of the genetic defect in a large cohort of IP patients and identification of novel NEMO mutations interfering with NF-kappaB activation. *Hum Mol Genet* **13**, 1763-73.

Legends to figures

Figure 1. NEMO domain organization and sequences of the synthetic zinc finger peptides. (a) Schematic representation of the structural motifs of NEMO. The predicted coiled-coils (CC1, CC2) and leucine zipper (LZ) motifs are represented by open boxes, and the zinc finger motif (ZF) by an open circle. Sequence numbering is given for hNEMO. The function of crucial regions is indicated on the top. **(b)** Sequence of the wild type (ZF-WT) synthetic zinc finger peptide. Zinc chelating Cys and His residues are highlighted in yellow, and highly conserved residues among classical zinc fingers in green. Residue Y11 (referred as “aromatic swap”), highlighted in magenta, also corresponds to a highly conserved aromatic residue, although more commonly found at position 13 in classical fingers. Two prolines in

the original sequence are replaced by two serines (underlined) to avoid eventual cis/trans isomerization. The pathogenic mutant (ZF-C417F) zinc finger contains the C417F mutation indicated by an arrow. ZF sequence numbering used in this study and corresponding hNEMO numbering are indicated on the top and bottom, respectively. Synthetic peptides are termini-blocked by N-acetyl (Ac) and C-amide (NH_2) groups.

Figure 2. Zinc-induced folding of the wild type and mutant zinc fingers. Amide/aliphatic regions of 2D-TOCSY spectra at 25°C of ZF-WT **(a)** and ZF-C417F **(b)** in the absence (red) and presence (black) of 2 molar equivalents of zinc. Assignments of the zinc-bound forms of both peptides are indicated by dotted lines and are given for the H^N/H^α connectivities (blue labels). Cross-peaks that appear below the threshold are shown with blue crosses (x). Assignment of unfolded peaks that are still visible after addition of zinc is indicated in red with the "u" superscript. Second (and eventually third) minor conformations in ZF-WT indicated by green asterisks are due to local conformational exchange occurring within the folded state.

Figure 3. Affinities of the wild type and mutant peptides for zinc. Zinc titration of ZF-WT (filled circles) and ZF-C417F (open circles) at 25°C and pH 7.3 monitored by fluorescence emission change of Y11 at 307 nm, after excitation at 285 nm. Fluorescence measurements were carried out using peptide concentrations of 1 μM, as described in Materials and Methods. The dissociation constants (K_D) extracted from non-linear least square fitting (solid line) are 0.3 ± 0.1 μM for ZF-WT and 0.7 ± 0.2 μM for ZF-C417F, with a stoichiometry of 1.0 ± 0.2 for both peptides. *Inset,* fluorescence emission spectra of ZF-WT (1 μM) in the absence (dashed line) or in the presence (solid line) of a saturating amount of Zn^{2+} (10 μM $ZnSO_4$).

Figure 4. Solution structure of NEMO wild type zinc finger and comparison to classical fingers. (a, b) Ribbon representation of a representative structure on top of the NMR ensemble. The zinc atom and ligating side chains (C6, C9, H22, C26) are shown in yellow, conserved residues (F4, L19) in green, the aromatic swap (Y11, A13) in magenta and V23, M24 and E25 in orange. Tyrosine Y11 hydroxyl group is shown in red and lysine K8 in blue, with its ε-amino group in cyan. **(c)** Superposition of ZFY-6 (CCH$\underline{H}_{27}$, pdb code **5znf** [37], blue), FOG-F3 (CCH$\underline{H}_{26}$, **1srk** [43], green) and USH-F9 (CCH$\underline{C}_{27}$, **1fu9** [30], grey) onto NEMO ZF (CCH$\underline{C}_{26}$, red). Backbone pairwise RMSD (sequence identity) to NEMO ZF for residues 4-26 are 0.66 Å (23.1 %), 1.00 Å (16.7 %) and 1.41 Å (16.7 %), respectively. Side chains are depicted for the zinc-chelating residues (balls and sticks), for the "conserved" residues at position 4, 19 (thick sticks) and for the aromatic residue (thin sticks) at position 11 ("swap") or 13 ("consensus").

Figure 5. Solution structure of the C417F mutant zinc finger. (a, b) Ribbon representation of a representative structure of ZF-C417F on top of the NMR ensemble. The same color-coding as in Figure 4(a) is used. Side chains of the highly flexible C-terminal residues (V23, M24, E25) and of the F26 mutated residue are shown in orange and yellow, respectively. The backbone carbonyl group of H22 is represented as red ball and stick. A water molecule probably stabilizing the zinc-coordination site (see text) is shown as red/white balls and sticks.

Figure 6. Thermal stability of the wild type and C417F mutant zinc fingers. Thermal denaturation curves of ZF-WT (filled circles) and ZF-C417F (open circles) peptides at concentration of 75 μM monitored by far-UV CD. Ellipticity was recorded at 222 nm and

converted to differential extinction coefficient per residue (Δε). For ZF-WT, the melting temperature (T_m) is above 90°C. For ZF-C417F, data were fitted to a two-state model (red line), yielding a T_m of 48.8 ± 0.4 °C and a cooperativity of 4.8 ± 0.2 (see Materials and Methods). *Inset*, far-UV CD spectra of ZF-WT (filled circles) and ZF-C417F (open circles), recorded at 1°C and concentration of 21 μM and 41 μM, respectively. A decrease in both positive and negative dichroic bands and a slight blue shift of the minimum at 206 nm (~ 1.5 nm) are observed in ZF-C417F, consistent with a decrease in helical content by about 8 %.

Figure 7. Incidence of the pathogenic C417F mutation on NF-kB activation. (a) Western blot showing hNEMO expression level in extracts of transiently transfected 293T cells. Note that endogenous NEMO was detected in mock-transfected cells. Each transfection was made in duplicate, and nucleotide diphosphate kinase (*NDPK*) was immunoblotted as a loading control. **(b)** Transient transfections. 1.3E2 and JM4.5.2 NEMO-deficient cells were co-transfected with the reporter plasmid Igκ-luciferase and with an empty vector (Control, C) or with an expression vector encoding either wild type (WT) or mutant (C417F) *hNEMO*. 1.3E2 and JM4.5.2 cells were stimulated during 6 h with 15 μg/ml LPS or 20 ng/ml IL-1β, or 4h with 10 ng/ml TNF-α, respectively. The NF-κB pathway activation corresponding to the ratio of luciferase activity in cell extracts in the presence and absence of the stimulus is taken as 100% activity for WT hNEMO. Absolute activation values for WT NEMO were 14.9 ± 2.6 fold for LPS, 15.7 ± 6.7 fold for IL-1β and 24 ± 8.5 fold for TNF-α. Error bars represent the standard deviation over four experiments.

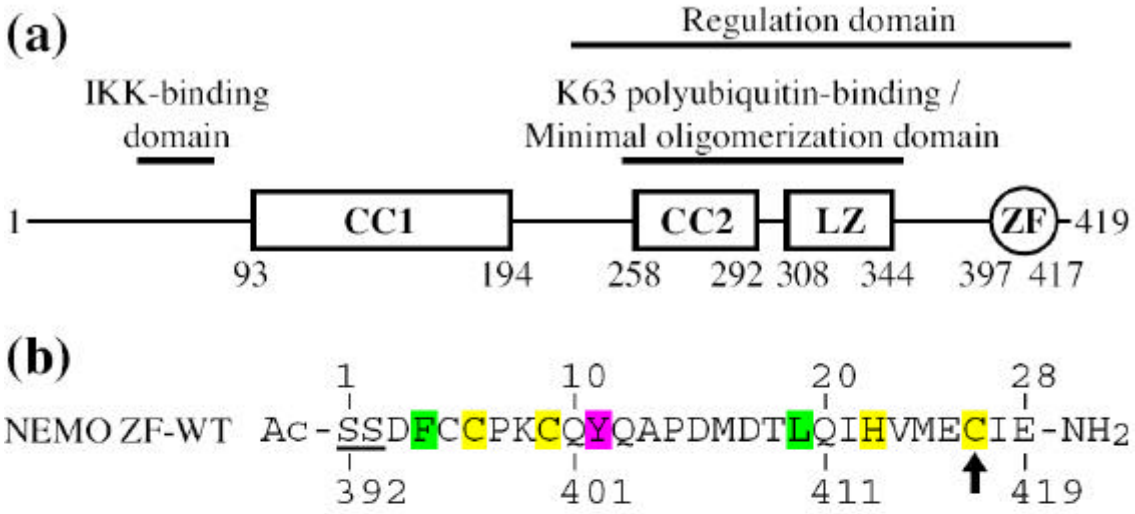

Figure 1. Cordier et al.

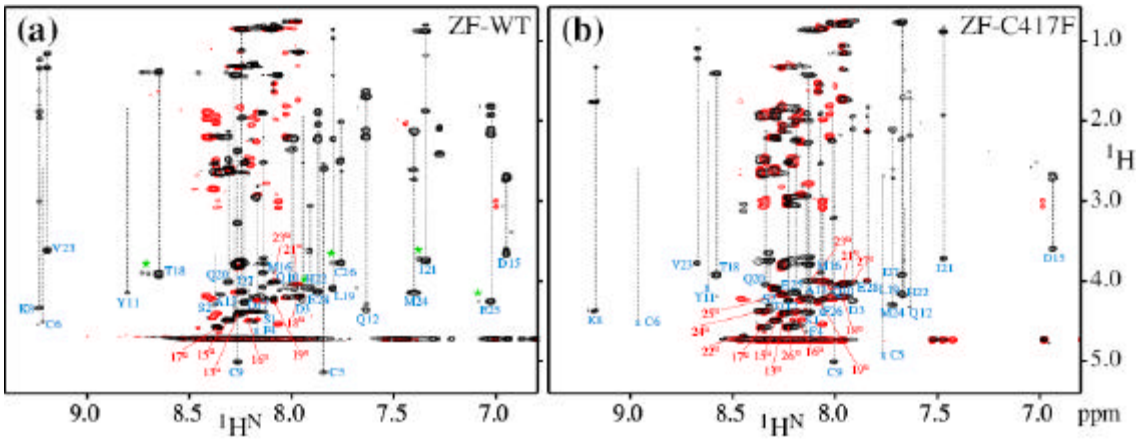

Figure 2. Cordier et al.

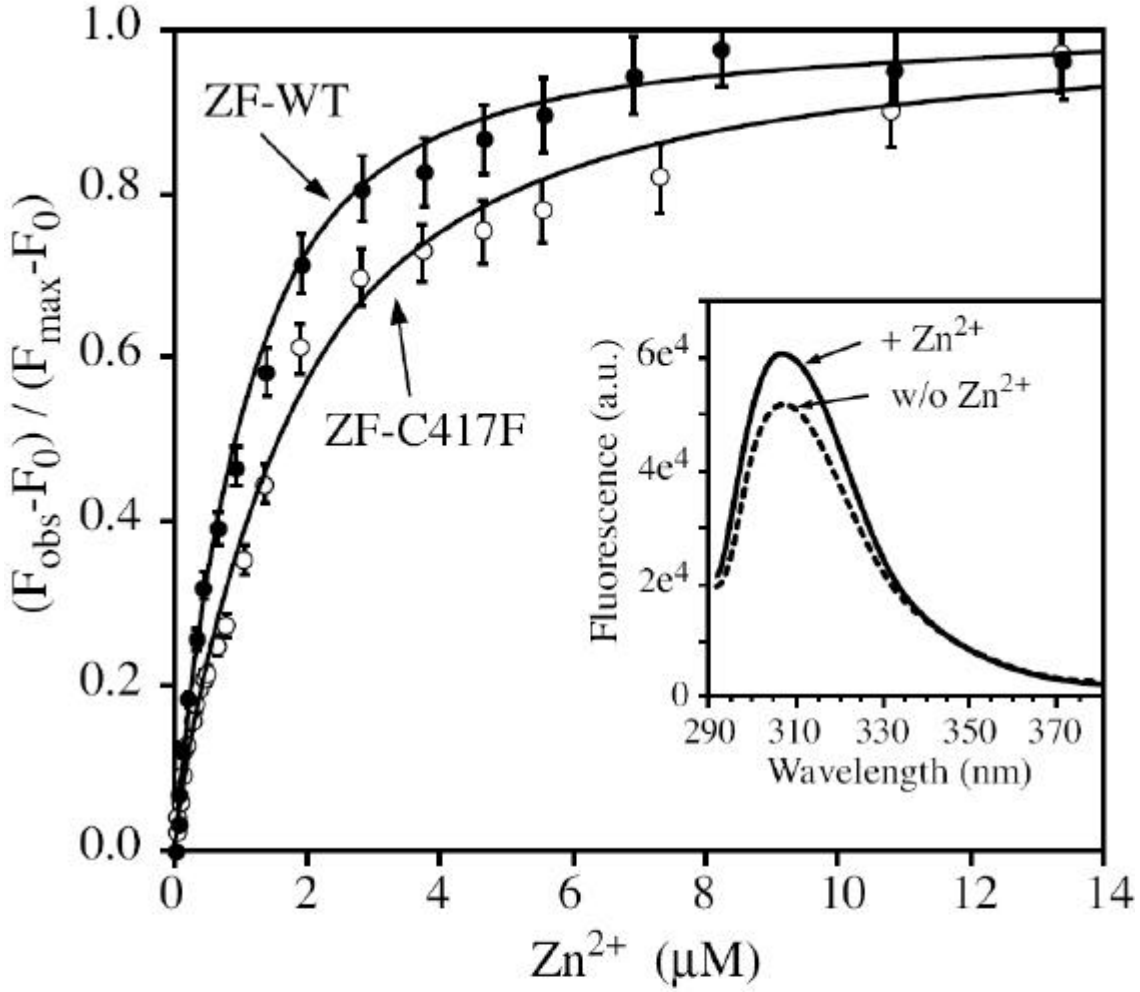

Figure 3. Cordier et al.

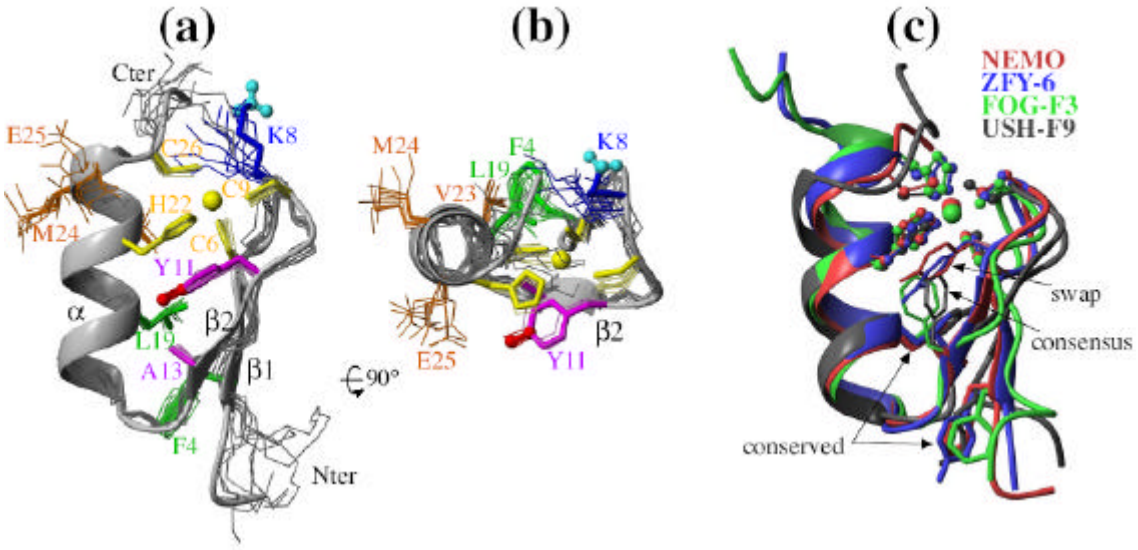

Figure 4. Cordier et al.

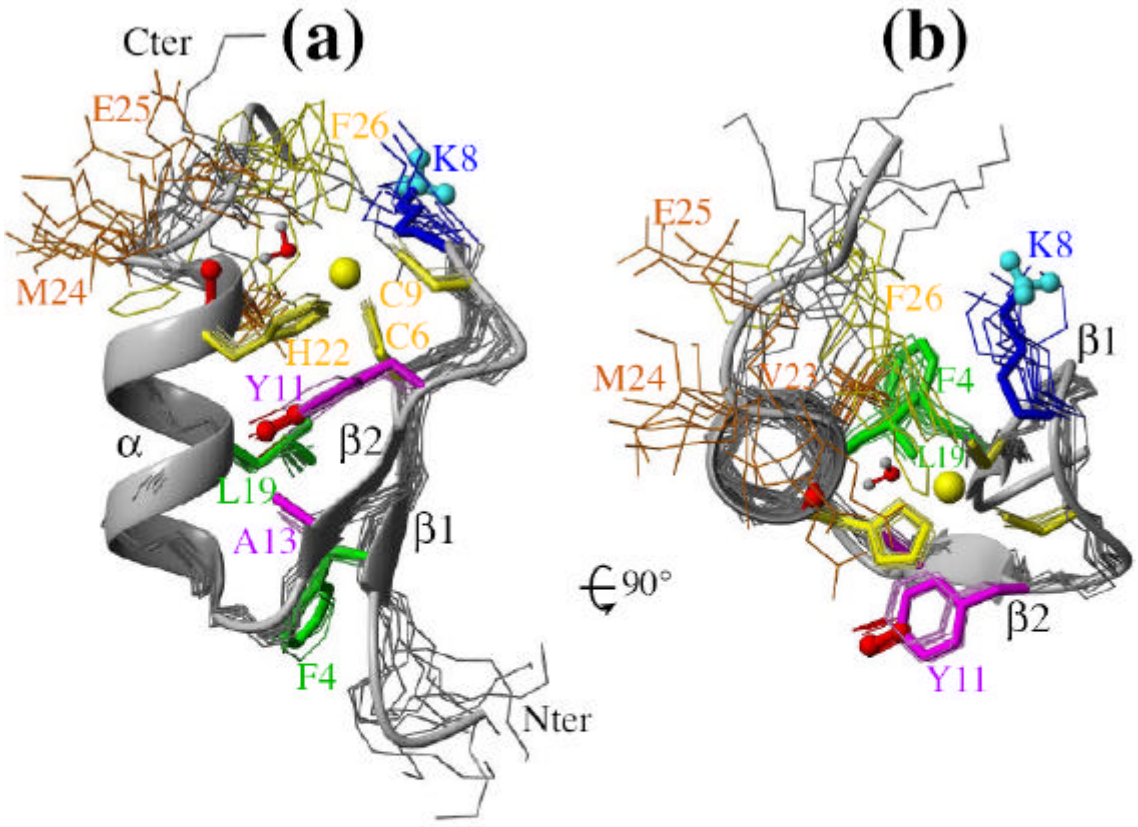

Figure 5. Cordier et al.

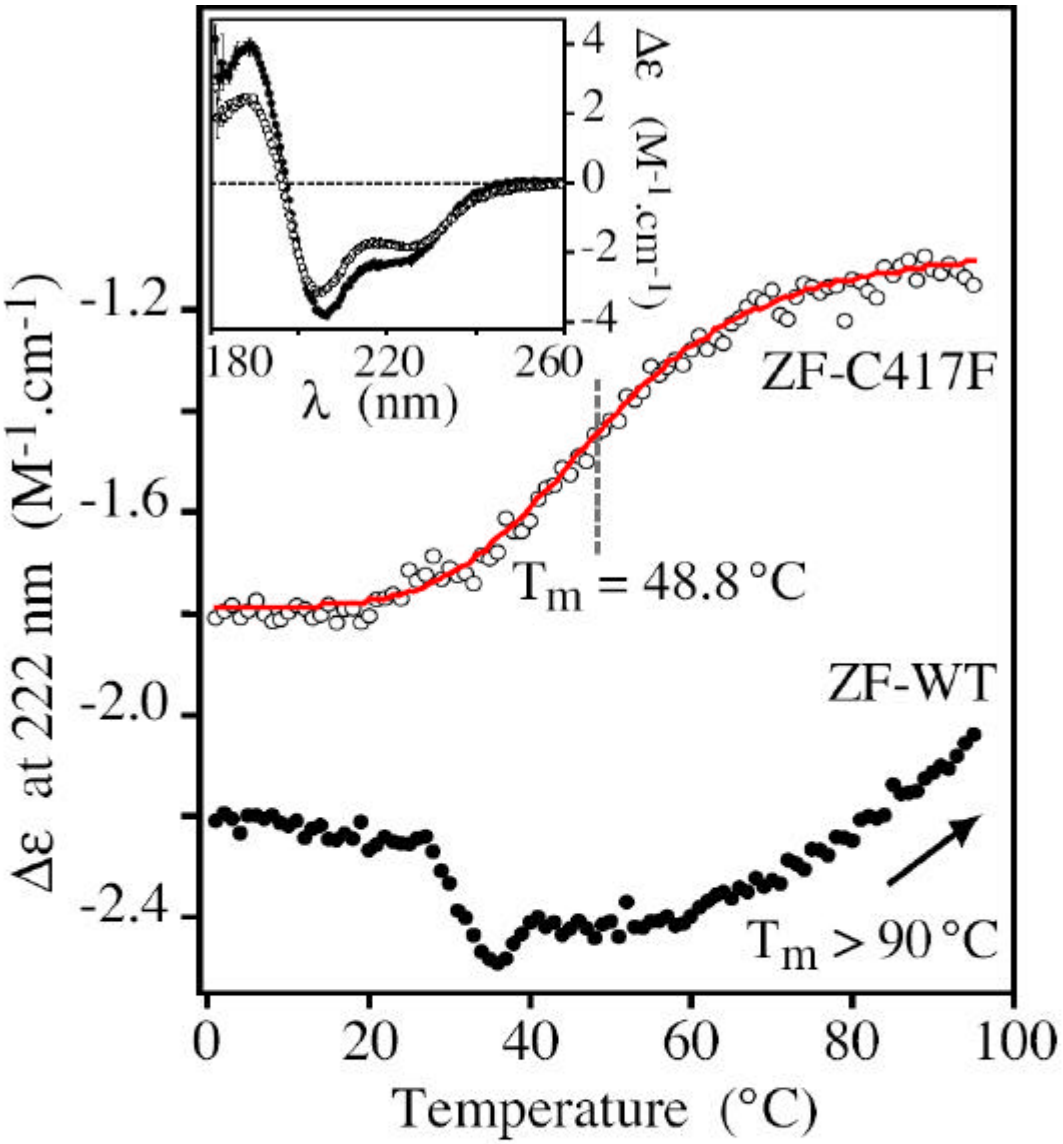

Figure 6. Cordier et al.

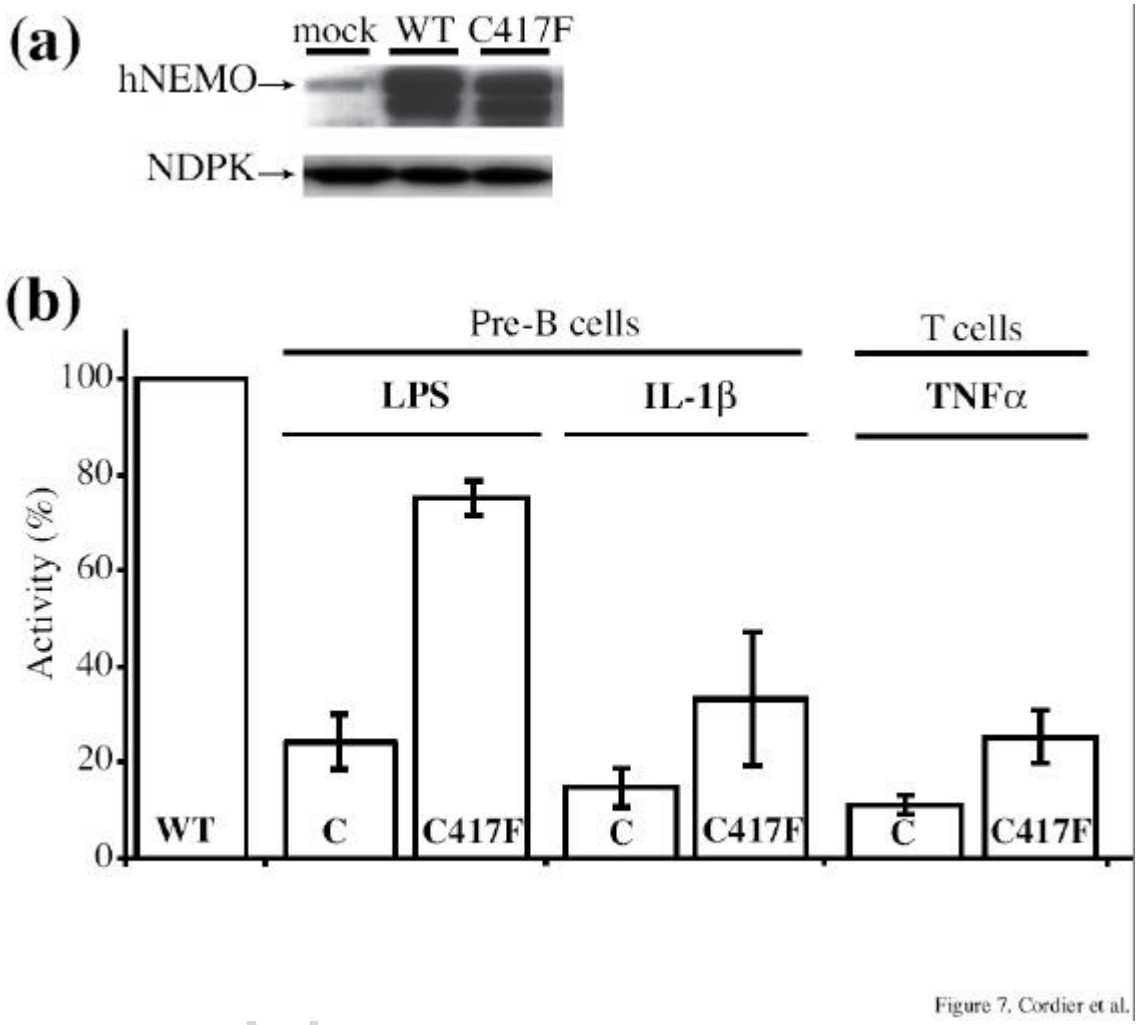

Figure 7. Cordier et al.